

## ScO<sub>x</sub> rich surface terminations on lanthanide scandate nanoparticles

Z. R. Mansley<sup>1</sup>, R. J. Paull<sup>1</sup>, E. P. Greenstein<sup>1</sup>, J. G. Wen,<sup>2</sup> K. R. Poeppelmeier,<sup>3</sup> and L. D. Marks<sup>1,\*</sup>

<sup>1</sup>Department of Materials Science and Engineering, Northwestern University, Evanston, Illinois 60208, USA

<sup>2</sup>Center for Nanoscale Materials, Argonne National Laboratory, 9700 S. Cass Ave., Lemont, Illinois 60439, USA

<sup>3</sup>Department of Chemistry, Northwestern University, Evanston, Illinois 60208, USA



(Received 8 July 2021; accepted 24 November 2021; published 23 December 2021)

The lanthanide scandate materials are widely used substrates for thin film growth and the potential applications of the  $Ln\text{ScO}_3$  materials continue to grow with the recent ability to synthesize them as cuboidal faceted nanoparticles. A comprehensive understanding of the surface structure and chemistry of these oxides is essential for their informed application, either as single crystal or high surface area nanoparticle substrates. Here the {100} pseudocubic surfaces of  $Ln\text{ScO}_3$  ( $Ln = \text{La, Nd, Sm, Gd}$ ) nanoparticles were examined with aberration-corrected electron microscopy and higher-level density functional theory to reveal ScO<sub>x</sub> rich terminations across all investigated surfaces. Mixed terminations of single and double layer nature were observed, indicating the presence of multiple domains at the surface and introducing the possibility of synthetically controlling the surface reconstruction in the future.

DOI: 10.1103/PhysRevMaterials.5.125002

### I. INTRODUCTION

For metals and simple semiconductors such as Si, Ge, and III-V compounds the surfaces are fairly well established. For oxides less is known. While it is convenient to consider that oxide surfaces are simple bulk truncations with perhaps some oxygen vacancies, there is now overwhelming evidence that this is rarely the case. The archetypal perovskite strontium titanate has been extensively studied, and the double-layer reconstructions [1] are now well established; an overview including an analysis of how these oxides conform to Pauling's rules [2], which in its modern form is considered via bond valence sums (BVS) [3–6], has been recently published by Andersen *et al.* [7]. Knowledge of the surface structure is critical in many areas: the surface plays a role in properties such as chemical adsorption, in catalysis, and beyond. For example, for LaTiO<sub>3</sub> films grown on SrTiO<sub>3</sub> with a double layer TiO<sub>2</sub> termination, the excess TiO<sub>2</sub> layer migrates to the surface of the film [8].

Complicating understanding of oxide surfaces are issues with how to prepare samples and avoid the highly reducing conditions often encountered in vacuum, and also how to determine the surface structure. Many techniques are surface sensitive, but only diffraction or imaging based methods are able to uniquely determine structures. Among these, high resolution electron microscopy in the profile mode was one of the first imaging methods used to solve surface structures [9–11], and has seen a recent increase of interest [12–18] due to improvements with aberration-corrected microscopes.

The lanthanide scandates have seen significant research interest as epitaxial substrates for film growth [19–24], and a recently developed technique to synthesize them as faceted

nanoparticles [25,26] has expanded their potential to applications as high surface area supports. This paper focuses upon determining the surface structure of lanthanide scandates on these faceted nanoparticles using profile imaging in an aberration-corrected microscope and coupling these experimental results with higher-level density functional calculations. It is relatively easy to satisfy valence neutrality in oxides such as strontium titanate where all atoms have an even valence. In contrast, the lanthanide scandates ( $Ln\text{ScO}_3$ ) contain cations with odd valence so there are less possibilities, and simple bulk truncations are always polar so there are significant open questions about the surface structure of these materials.

The  $Ln\text{ScO}_3$  materials typically adopt the  $Pbnm$  orthorhombic perovskite structure, which can be conveniently described using two, stacked pseudocubic units defined by the {110} and (002) planes in each unit cell. The atomic layers in these directions are either ScO<sub>2</sub><sup>-</sup> or  $Ln\text{O}^+$ , and this uneven valence makes a bulk termination impossible. These pseudocubic units have lattice parameters ranging from 4.05 Å for LaScO<sub>3</sub> [27] to 3.95 Å for DyScO<sub>3</sub> [28], making the library of lanthanide scandates excellent substrate candidates for studying strain related phenomena in both noble metals and various oxides (e.g., the generation of room temperature ferroelectricity in SrTiO<sub>3</sub> [22]).

Turning to  $Ln\text{ScO}_3$  nanoparticles in Fig. 1, the low order pseudocubic faces dominate their surfaces indicating these will drive observed surface properties and must be understood for informed application of these substrates. The (110) surface has been previously studied on commercially available (110) oriented single crystals [29–32] and recent work revealed a (1×1) double layer termination consisting of scandium and oxygen, which was additionally observed on GdScO<sub>3</sub> and DyScO<sub>3</sub> nanoparticles [33]; however, this is a narrow window of the accessible lanthanide scandate materials and surfaces.

\*Corresponding author: l-marks@northwestern.edu

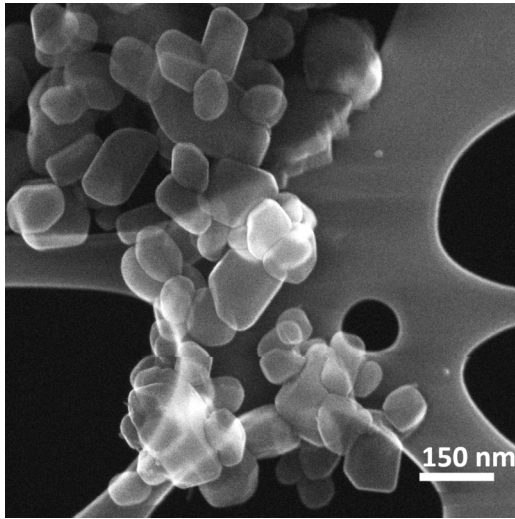


FIG. 1. Secondary electron image of  $\text{NdScO}_3$  supported on lacy carbon. Other  $\text{LnScO}_3$  nanoparticles were similar.

Here we expand this work to explore nanoparticle surfaces of additional lanthanide cations including La, Nd, and Sm; as well as the other pseudocubic face, the (001). While the (001) and  $\{110\}$  planes are both major pseudocubic faces,  $\{100\}_{\text{pc}}$ , there are minor differences between the two in terms of symmetry and octahedral rotations below the surface, indicating both surfaces must be individually studied. The result is a chemically, electronically, and structurally similar surface across the majority of facets of  $\text{LnScO}_3$  nanoparticles, ideal for systematic studies across multiple supports.

## II. METHODS

The  $\text{LnScO}_3$  nanoparticles were synthesized using the hydroaqua method described by Paull *et al.* [25,26] which is a sol-gel process with a two-step heating cycle in a humid environment to promote facetting [34]. These samples were observed using both scanning transmission electron microscopy (STEM) and Cs/Cc corrected high resolution transmission electron microscopy (HREM). The STEM was performed on a Hitachi HD2300 operated at 200 kV using a secondary electron detector to determine particle morphology. HREM was carried out on the Argonne Chromatic Aberration-corrected TEM (ACAT), a FEI Titan 80–300 modified with both Cs and Cc image correction, operated at 200 kV. Profile images [10] of the particle surfaces were obtained by orienting the nanoparticles to either  $\langle 100 \rangle$  or  $\langle 110 \rangle$  pseudocubic directions. These images were then compared to simulations of density functional theory (DFT) predicted structures using the MacTempasX software package for multislice and nonlinear imaging simulation with parameters matching ACAT working conditions (200 kV,  $<15 \mu\text{m} \text{C}_s$ , 40-nm focal spread).

DFT calculations were performed to explore and relax the atomic positions of various candidate surface structures using the all-electron augmented plane wave+local orbitals WIEN2K package [35,36] with on-site hybrids [37,38] and the PBEsol functional [39]. As discussed previously [33,40–42], the  $\text{LnScO}_3$  system is adequately described using on-site hybrid fractions of 0.38, 0.50, and 0.80 for the  $\text{Ln}$  4*f*,  $\text{Ln}$  5*d*,

and Sc 3*d* orbitals, respectively, and muffin-tin radii of 2.02, 1.82, and 1.68 for the  $\text{Ln}$ , Sc, and O atoms respectively. For the (001) double layer reconstructions we used a slab of 200 unique atoms with a cell of  $11.1 \times 11.6 \times 54.0 \text{ \AA}$ , approximately 14  $\text{\AA}$  vacuum, and a  $2 \times 2 \times 1$  *k*-point mesh for the  $(2 \times 2)$  structure. The  $(1 \times 1)$  calculation used 51 atoms, a  $5.5 \times 5.8 \times 54.0 \text{ \AA}$  slab, and a  $4 \times 4 \times 1$  mesh. The single layer terminations were modeled on the  $\langle 110 \rangle$  surface and used a slab of 115 atoms, a cell of  $70.3 \times 8.0 \times 8.0 \text{ \AA}$ , approximately 20  $\text{\AA}$  of vacuum and a *k*-point mesh of  $1 \times 4 \times 4$ . All calculations used  $P\bar{1}$  symmetry and a plane-wave expansion parameter RKMAX of 6.0. DFT optimized lattice constants were used throughout and the structure files can be found in the Supplemental Material [43]. Atomic positions were minimized and converged using a quasi-Newton algorithm [44]. We utilized ferromagnetic ordering and did not treat spin orbit coupling of the valence states (it is automatically included for the core states).

## III. RESULTS

Figure 1 is a representative secondary electron image of the  $\text{LnScO}_3$  nanoparticles, showing their size and faceted nature. Additional images of these faceted nanoparticles can be found in Refs. [25,26]. The surface was found to contain a double layer termination (Fig. 2) on a majority of the surfaces as well as scattered regions of single layer terminations (Fig. 5, discussed later). We will first discuss the double layer termination.

### A. Double layer termination – $\langle 110 \rangle$ surface

HREM images of the particle surfaces in profile view are shown in Fig. 2. Observed along a  $\langle 110 \rangle_{\text{pc}}$  direction, the double layer surface is clear and similar across the four  $\text{LnScO}_3$  materials studied here. Multislice simulation based on the reported  $\langle 110 \rangle$  structure [33,41,42] is overlaid in Fig. 2(c), demonstrating a reasonable match between the surfaces of nanoparticles and previously studied single crystals. The simulation is for a total thickness of 45 nm, which is approximately the sample thickness based upon the shape of the nanoparticles; while it is possible to refine accurately positions from profile images (e.g., Refs. [9,12]), this requires thin samples which the synthesis did not produce. We should note that simulations for higher thicknesses are known to be less accurate since it is hard to correctly include inelastic scattering as well as reduction in coherence due to phonon scattering, as just two of what are known to be a limitation of quantitative high-resolution imaging for thicker crystals.

The surfaces were also imaged down the  $\langle 100 \rangle_{\text{pc}}$  directions as shown in Figs. 2(e) and 2(f). While the double layer is not so obvious along  $\langle 100 \rangle_{\text{pc}}$  zone axes and the particle morphology results in rather large thicknesses, the motif at the surface is the same while the bulk motif has rotated 90 degrees indicating a double layer reconstruction exists on both the  $\langle 110 \rangle$  and the previously unstudied  $\langle 001 \rangle$  surface. For reference, the images can be compared to the single-layer images shown later in Fig. 5, and it is clear by inspection that they are very different. A larger scale comparison of Fig. 2(c) is included in the Supplemental Material [43], and also the ball-and-stick

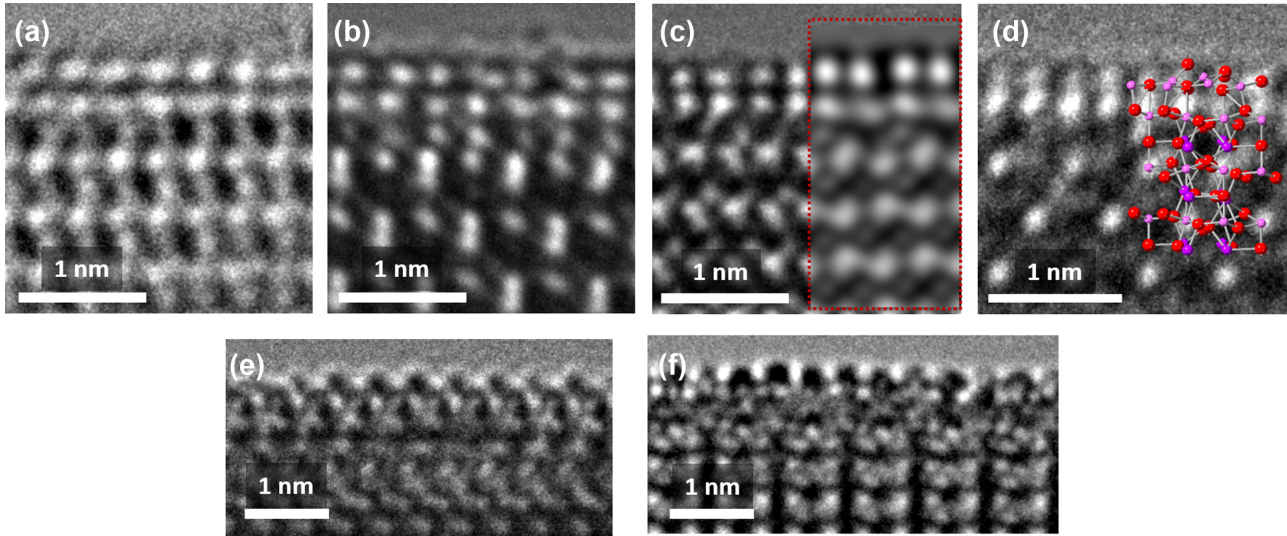


FIG. 2. Aberration corrected TEM images of nanoparticle surfaces. (a)–(d) are views along a pseudocubic  $\langle 110 \rangle$  zone axis of LaScO<sub>3</sub>, NdScO<sub>3</sub>, SmScO<sub>3</sub>, and GdScO<sub>3</sub> respectively. (e) and (f) are along a pseudocubic  $\langle 100 \rangle$  axis of the similar (001) surface of LaScO<sub>3</sub> and the (110) surface of GdScO<sub>3</sub>. Multislice simulation based on the predicted double layer structure is overlaid in (c) and shows a reasonable match, and a ball-and-stick model is overlaid on (d) (red atoms are O, pink are Sc, and purple Gd). (d) and (f) are adapted and reproduced [33].

model in Fig. 2(d) along with its polyhedral representation. The bulk of the structure does not simply project along the beam direction, so the ball-and-stick models are never going to be good representations compared to the polyhedral representation; however the ball-and-stick model does allow for easier visualization of the aligned rows of O and Sc atoms at the surface.

### B. Double layer termination – (001) surface

Because the images are projections along the beam direction, there is some ambiguity about the atom positions along this direction; it is unconditional that the surface has a double-layer structure. To clarify this DFT was used to explore potential double layer (001) surface reconstructions. While similar, these surfaces are symmetrically distinct from each other, and the (001) surface must be considered on its own to explore any potential differences in the surface reconstruction. Atomic arrangements with both  $(1 \times 1)$  and  $(2 \times 2)$  symmetries that maintained the allowed valence neutral stoichiometry and adhered to Pauling's Rules, which have been shown to apply to surface reconstructions [7], were assessed. In effect the DFT is being combined with the constraints of the experimental images, the absence of any larger unit cell reconstruction as well as valence neutrality constraints consistent with how the samples were produced.

Figure 3 shows the lowest energy solutions for both the  $(1 \times 1)$  and  $(2 \times 2)$  reconstructions of the (001) surface of GdScO<sub>3</sub>. These reconstructions are stoichiometrically identical and only vary in the positioning of the ScO<sub>x</sub> polyhedra, which consist of ScO<sub>4</sub> (red), ScO<sub>5</sub>[ ] (blue, we include the “[ ]” to indicate this unit is similar to a ScO<sub>6</sub> unit with a vacancy), and ScO<sub>6</sub> (pink). Where the  $(1 \times 1)$  is dominated by longer rows of polyhedral units, those same polyhedra are periodically offset in the  $(2 \times 2)$ , allowing for more corner sharing and Sc relaxation into the bulk where it can coordinate with 6 O atoms. This relaxation also affects the subsurface ScO<sub>6</sub>

units (gray), which are vertically stretched in the  $(1 \times 1)$  but more symmetric in the  $(2 \times 2)$ . As a result of these favorable relaxations, the  $(2 \times 2)$  structure is predicted to be lower in energy by 549 meV per pseudocubic unit (this is denoted as meV/PC unit hereafter, recall the full *Pbnm* structure contains 2 pseudocubic units).

The other potential polyhedral arrangements of the double layer reconstructions are close in energy as shown in Table I with corresponding crystallographic information files (CIFs) in the Supplemental Material [43]. Multislice simulations of the solutions labeled 2a, 2b, and 2e in Table I are also included in the Supplemental Material (these structures were selected to represent the two low energy solutions as well as one modeled after the (110) double layer for comparison) [43]. They

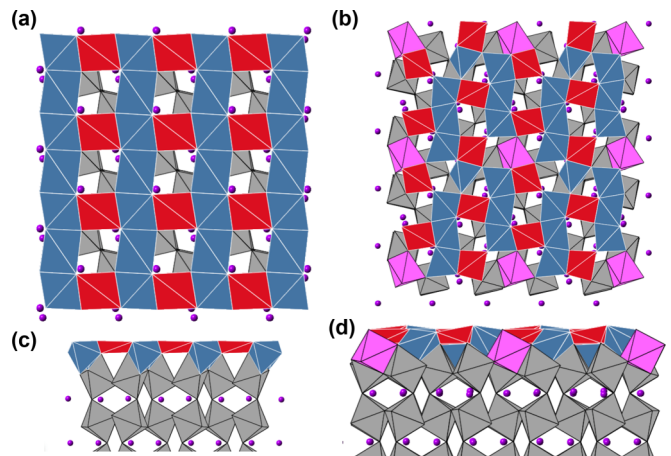


FIG. 3. DFT relaxed structures for the lowest energy  $(1 \times 1)$  [(a) and (c)] and  $(2 \times 2)$  [(b) and (d)] reconstructions on the (001) surface. (a) and (b) show plan view images while (c) and (d) show the  $[010]$  view direction. Grey polyhedra are ScO<sub>6</sub> units in the bulk, pink are ScO<sub>6</sub> at the surface, blue are ScO<sub>5</sub>[ ], and red are ScO<sub>4</sub>. The purple atoms are Gd.

TABLE I. Energy differences compared to the minimum energy structure of various surface polyhedral arrangements on  $\text{GdScO}_3$ . Structures 2a-2g represent the  $(2 \times 2)$  structures and 1a/1b are the  $(1 \times 1)$ . Structures 2a-2d are translations of the low energy solution in Figs. 3(b) and 3(d), and 2e-2g are motifs based on the solved  $(110)$  structure, which is shown to be comparatively unfavorable on this surface. Structure naming corresponds to the CIF files in the Supplemental Material [43].

$(2 \times 2)$ structure	Energy difference (meV/PC unit)
2a	0
2b	84
2c	191
2d	204
2e	3169
2f	3921
2g	5935
1a	549
1b	908

are quite similar both to each other and to the  $(110)$  double layer simulation overlaid in Fig. 2(c) as expected, though the contrast at the surface of the  $(2 \times 2)$  simulations is more diffuse than the  $(110)$  due to the atomic relaxations on the  $(001)$  surface.

At room temperature  $k_b T$  is approximately 25 meV, and compounded with the added enthalpy and entropy of the hydrosauna synthesis environment we propose the surface contains either (1) combinations of short range domains of structure 2a with some domains of 2b, or (2) the surface is disordered with respect to which of the potential vacant sites is occupied to achieve valence neutrality in a given area while facilitating the favorable structural relaxations (though a number of challenges exist in assessing (2) via DFT).

Figure 4 shows the projected density of states (pDOS) of the Sc 3d orbitals delimited by polyhedral unit for the

low energy solutions on  $\text{GdScO}_3$  and  $\text{NdScO}_3$ , as well as a comparison between the O 2p and  $\text{Ln}$  4f surface and bulk states. Considering the similarities between the  $\text{LnScO}_3$  materials in imaging, as well as the similarities between  $\text{SmScO}_3$ ,  $\text{GdScO}_3$ , and  $\text{DyScO}_3$  [33] in DFT, we expect similar features in all of the  $\text{LnScO}_3$  materials, and this is indeed the case. In fact, when considering the Sc and O atoms in  $\text{GdScO}_3$  and  $\text{NdScO}_3$ , the surface states are more similar to each other than to their respective bulk states. Note that the  $\text{Ln}$  4f shows very little change between the bulk- and surface-most Ln atoms; below the outermost surface layer, the structure is nearly congruent to the bulk structure with minor positional relaxations, and has almost the same electronic structure.

Compared to the pDOS of the  $(110)$  surface reported previously [33], the electronic structure is quite similar. The O 2p and  $\text{Ln}$  4f dominate the filled states in the valence band, and the unoccupied states in the conduction band consist mainly of Sc 3d states. Additionally, there is evidence of an in-gap state (with respect to the bulk bandgap) in the unoccupied Sc 3d approximately 4 eV above the valence band maximum attributed to the tetrahedral  $\text{ScO}_4$  units (red in Figs. 3 and 4). There is minimal difference between the DOS of the bulk and the surface.

### C. Single layer termination

A single layer reconstruction was observed alongside the double layer, shown in Fig. 5. These half-unit cell steps only appear sparsely in imaging; from HREM imaging we estimate that  $\sim 10\%$  of the synthesized surfaces have this single layer termination. Visual inspection compared to the neighboring atomic layers and reconstruction indicates a bulk-like termination, but a bulk single layer termination at the  $\text{ScO}_2^-$  layer is not valence neutral. While valence neutrality for a surface can be realized through methods such as adsorption (e.g., with a  $\text{H}^+$ ), it can also be achieved here through the removal of 0.25 O atoms, or 1 O atom in a  $\text{Sc}_4\text{O}_4^-$  unit of the surface.

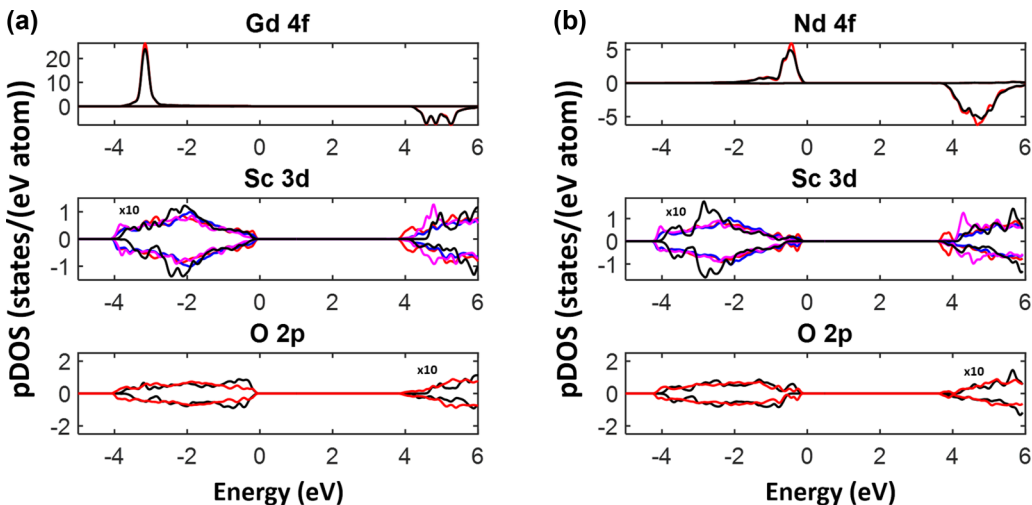


FIG. 4.  $\text{Ln}$  4f, Sc 3d, and O 2p pDOS from the  $(2 \times 2)$  reconstruction on  $\text{GdScO}_3$  and  $\text{NdScO}_3$  (001). Black lines represent the innermost atoms of the slab and show good agreement to bulk calculations [33]. For the  $\text{Ln}$  and O pDOS, the red lines indicate the surface atoms. In the Sc pDOS, the red represents surface  $\text{ScO}_4$  polyhedra, blue  $\text{ScO}_5[]$ , and pink  $\text{ScO}_6$  (corresponding to polyhedral colorings in Fig. 3). The occupied Sc 3d and unoccupied O 2p states are amplified by a factor of 10 as indicated for visibility.

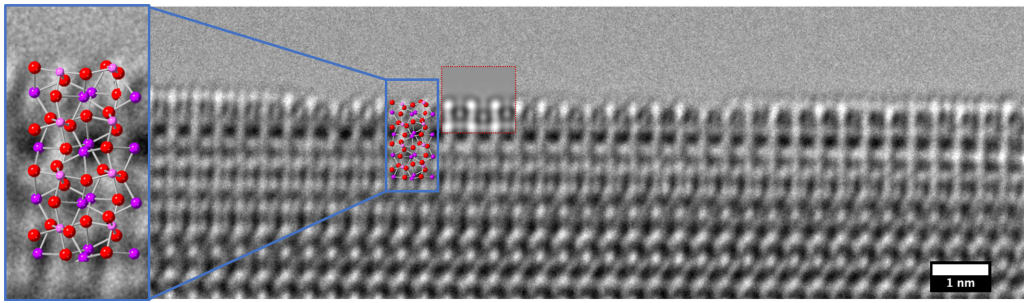


FIG. 5. Aberration corrected HREM of an LaScO<sub>3</sub> (001) surface showing a region of single layer termination in the center. Multislice simulation based on the predicted structure for a thickness of 5 nm (this particular nanoparticle was quite thin at the surface with a sharp increase in thickness moving into the bulk) is overlaid with a red outline and shows good agreement at the surface. A ball-and-stick model is also overlaid and a magnified view is included on the left for visibility, outlined in blue.

This gives a surface chemistry of Sc<sub>4</sub>O<sub>7</sub><sup>-2</sup>, which reduces to ScO<sub>1.75</sub><sup>-0.5</sup> per pseudocubic unit, resulting in valence neutrality when balanced with the subsurface LnO<sup>+</sup> layer.

The potential oxygen deficient structures that maintain a bulklike ordering (consistent with the images) were assessed with DFT and the results are reported in Table II with corresponding CIF files in the Supplemental Material [43]. The minimum energy solution is shown in Fig. 6(a) and multislice simulation based on that structure is a good match to the experimental image at the surface (Fig. 5). It should be noted that the structure shown in Fig. 6(a) is calculated on the (110) surface, and we expect the (001) to be very similar but with slight differences in polyhedral arrangement analogous to the double layer (110) and (001) structures. The pDOS of the single layer surface termination was also calculated and is reported in Fig. 6(b). There are some differences that now appear in the Gd 4f as it is closer to the surface. Additionally, there is a shift in the valence band maximum due to occupied states in the surface O 2p. Overall the changes are relatively small.

#### IV. DISCUSSION

Despite symmetry differences and varying octahedral tilts, the (001) and (110) planes of the LnScO<sub>3</sub> materials are similar in terms of atomic positions and layer chemistry. Each plane is either LnO<sup>+</sup> or ScO<sub>2</sub><sup>-</sup> so comparable valence balancing behavior for both surfaces is expected, and that is the case with these surface terminations. Though minor differences exist with regards to the exact atomic positions and occupancies, the stoichiometry and electronic structure of these

TABLE II. Energy differences compared to the minimum energy structure of the single layer reconstruction. Structures 1 and 2 are essentially equivalent.

Structure	Energy difference (meV/PC unit)
1	0
2	15
3	143
4	265
5	2478
6	2481

reconstructions are similar on both major pseudocubic faces of these materials, regardless of the Ln cation. Atomic positions will shift as the lattice parameter and octahedral tilts vary in magnitude, but the overall structure remains the same. In application, these surfaces can be viewed as nearly identical for all of the LnScO<sub>3</sub> (110) and (001) surfaces.

Although the (2×2) structure has significantly lower energy than the (1×1), consideration of both structures yields insight into the ways that surfaces minimize energy and why the (2×2) is preferred. In the (1×1), symmetry constraints lead to neat rows of polyhedra, but at the intersections of these rows the polyhedral unit is surrounded and shares four edges. The (2×2) staggers the ScO<sub>x</sub> polyhedra, which both allows the ScO<sub>x</sub> units to relax into more favorable positions that favor corner sharing and to coordinate with more oxygen atoms to form ScO<sub>6</sub> units in the (2×2) that is not seen in the (1×1). In addition to preferable polyhedral arrangement, this also mitigates the vertical elongation observed in the subsurface ScO<sub>6</sub> polyhedra in the (1×1).

Prioritizing corner sharing over edge and forming bulk like polyhedra (i.e., ScO<sub>6</sub> vs ScO<sub>5</sub>[]) follow directly from Pauling's third and fifth rules [2,7]. While these relaxations can be facilitated by regularly offsetting these rows as demonstrated by the (2×2), it can also be achieved through irregular changes in the occupation of these sites in a glass-like surface, or a surface with many local domains.

The single layer reconstruction mixed with the double layer on these nanoparticles is not surprising; complex oxide surfaces such as SrTiO<sub>3</sub> often show mixed surface reconstructions on the same surface [8,45,46]. Note that the surface stoichiometry is different, so the two different terminations do not compete; they can coexist without any scientific issues. Varying synthesis methods and processing can preferentially reconstruct these surfaces as well [12,32,47]. Previous work on the (110) single crystal surface did not indicate the presence of this single layer termination seen sparsely on the nanoparticles; though the double layer is still the preferred termination, the single layer is favorable enough during nanoparticle synthesis to coexist with the double layer.

One explanation for this is the varied atmospheres between the two syntheses; while the nanoparticles are synthesized in a humidified Ar atmosphere, the single crystals in the reference were treated in air at higher temperature [33]. Surface adsorbates influence the preferred surface termination, and

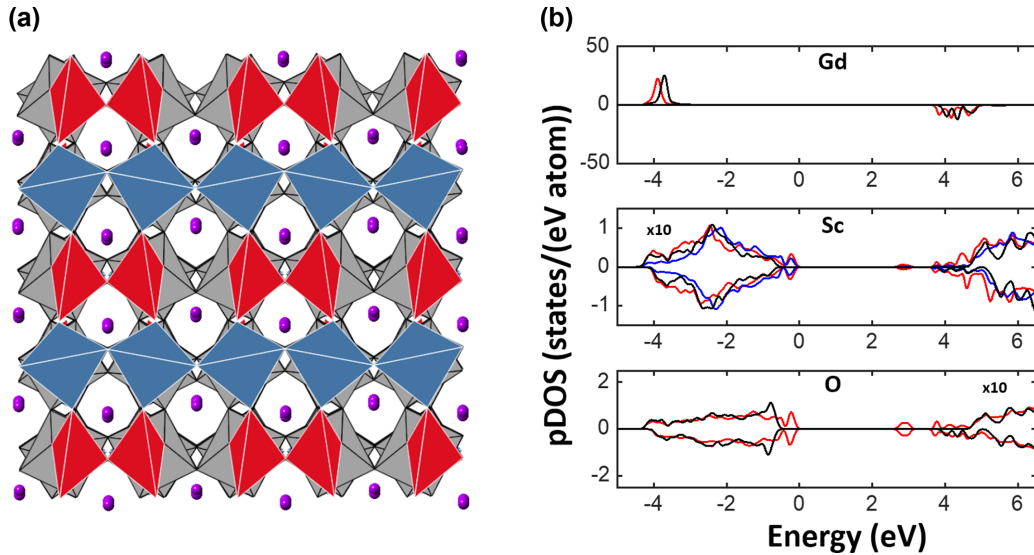


FIG. 6. (a) shows the DFT relaxed structure of the single layer reconstruction on  $\text{GdScO}_3$ , where the polyhedra are colored similarly to Fig. 3. The pDOS is plotted in (b) using the same convention as Fig. 4. Again, the occupied Sc  $3d$  and unoccupied O  $2p$  states are amplified by a factor of 10 as indicated for visibility.

even generate hydrated surface terminations in some material systems such as  $\text{MgO}$  [48–50] and  $\text{SrTiO}_3$  [51,52]. While we do not claim here that the single layer termination is hydrated, the presence of water in the synthesis environment can affect the surface compositions. Since the presence of this mixed reconstruction is influenced by the synthesis method, future refinement of the synthesis may be able to preferentially form either the single or double layer as the primary product.

A few other direct consequences of the results herein merit mention:

(1) The fact that the same reconstruction occurs across the  $\text{LnScO}_3$  series removes one potential variable across the series with the use of these materials as substrates for thin film growth or as heterogeneous catalyst supports. This has relevance in that for gold catalysts used for CO oxidation [53] the adhesion varies minimally across the lanthanide series, but the activation energy changes due to inductive effects from the  $4f$  electrons. Work in progress indicates that for Pt nanoparticles the lattice parameter and hence pseudomorphic strain across the series matters.

(2) In principle, one could transition between the single-layer and double-layer surfaces by varying the surface chemistry, for instance by changing how the initial growth is done. It may also be possible to transition by changing initial annealing conditions, both time and temperature, as this will effect surface segregation of point defects from the bulk.

(3) The presence of two  $\text{ScO}_x$  layers must be carefully considered when attempting to grow chemically controlled thin films. Either (a) the double layer remains at the interface as a second phase, different from what might be assumed in epitaxial models; (b) the excess Sc diffuses into the film, creating defects and altering the expected chemistry; or (c) it acts as a surfactant layer for homo- or heteroepitaxial growth.

(4) While the surfaces herein on pseudocubic faces are double-layer, they are significantly different from the (001)

double-layer reconstructions on  $\text{SrTiO}_3$ . The latter are built around tiling of  $\text{TiO}_5$  units [7,45,46], whereas herein the surfaces contain these and also tetrahedral  $\text{ScO}_4$  units, more similar to  $\text{SrTiO}_3$  (111) surfaces [7,54].

(5) Again similar to the surfaces of  $\text{SrTiO}_3$  and  $\text{BaTiO}_3$  nanoparticles [12,55,56], the nanoparticle reconstructions here are comparable to their single crystal counterparts [33]. There may also be coexisting double-layer reconstructions.

(6) As mentioned earlier [33] for the (110) surfaces of  $\text{LnScO}_3$  ( $\text{Ln} = \text{Gd}, \text{Tb}, \text{Dy}$ ) the surface structures described herein should be general for all 332 perovskites. This we can now extend to all the lanthanides, and also the (001) surfaces.

(7) Similar to (6), the single-layer structures can be assumed to be general, *iff* the chemistry is controlled.

## V. CONCLUSION

Through the theoretical and experimental study of  $\text{LnScO}_3$  nanoparticle surfaces, the major pseudocubic faces were shown to share Sc rich surface reconstructions across the lanthanide series. The most common structure seen is a Sc rich double layer, with a mix of an occasionally observed single layer surface termination.

## ACKNOWLEDGMENTS

This research was supported by funding from the Northwestern University Institute for Catalysis in Energy Processes (ICEP) from Grant No. DOE DE-FG02-03ER15457. Use of the Center for Nanoscale Materials, an Office of Science user facility, was supported by the U.S. Department of Energy, Office of Science, Office of Basic Energy Sciences, under Contract No. DE-AC02-06CH11357.

All authors contributed to the overall analysis and writing of the manuscript.

- [1] N. Erdman, K. R. Poeppelmeier, M. Asta, O. Warschkow, D. E. Ellis, and L. D. Marks, *Nature (London)* **419**, 55 (2002).in
- [2] L. Pauling, *J. Am. Chem. Soc.* **51**, 1010 (1929).
- [3] I. D. Brown and D. Altermatt, *Acta Cryst. B* **41**, 244 (1985).
- [4] I. D. Brown, in *International Union of Crystallography Monographs on Crystallography* (Oxford University Press, Oxford, 2002), p. 12.
- [5] I. D. Brown, *Chem. Rev.* **109**, 6858 (2009).
- [6] J. A. Enterkin, A. E. Becerra-Toledo, K. R. Poeppelmeier, and L. D. Marks, *Surf. Sci.* **606**, 344 (2012).
- [7] T. K. Andersen, D. D. Fong, and L. D. Marks, *Surf. Sci. Rep.* **73**, 213 (2018).
- [8] S. Cook, K. Letchworth-Weaver, I. C. Tung, T. K. Andersen, H. Hong, L. D. Marks, and D. D. Fong, *Sci. Adv.* **5**, eaav0764 (2019).
- [9] L. D. Marks, *Phys. Rev. Lett.* **51**, 1000 (1983).
- [10] L. D. Marks and D. J. Smith, *Nature (London)* **303**, 316 (1983).
- [11] L. D. Marks, *Surf. Sci.* **139**, 281 (1984).
- [12] Y. Y. Lin, J. G. Wen, L. H. Hu, R. M. Kennedy, P. C. Stair, K. R. Poeppelmeier, and L. D. Marks, *Phys. Rev. Lett.* **111**, 156101 (2013).
- [13] Y. Y. Lin, Z. L. Wu, J. G. Wen, K. R. Poeppelmeier, and L. D. Marks, *Nano Lett.* **14**, 191 (2014).
- [14] W. Zhang and W. T. Zheng, *Phys. Chem. Chem. Phys.* **17**, 14461 (2015).
- [15] W. T. Yuan, Y. Wang, H. B. Li, H. L. Wu, Z. Zhang, A. Selloni, and C. H. Sun, *Nano Lett.* **16**, 132 (2016).
- [16] W. T. Yuan, H. L. Wu, H. B. Li, Z. X. Dai, Z. Zhang, C. H. Sun, and Y. Wang, *Chem. Mat.* **29**, 3189 (2017).
- [17] M. Ek, I. Beinik, A. Bruix, S. Wendt, J. V. Lauritsen, and S. Helveg, *Faraday Discuss.* **208**, 325 (2018).
- [18] L. H. Liu, Z. Y. Cheng, J. Zhu, and R. Yu, *J. Phys. Chem. C* **124**, 16431 (2020).
- [19] C. H. Lee, V. Skoromets, M. D. Biegalski, S. M. Lei, R. Haislmaier, M. Bernhagen, R. Uecker, X. X. Xi, V. Gopalan, X. Marti, S. Kamba, P. Kuzel, and D. G. Schlom, *Appl. Phys. Lett.* **102**, 082905 (2013).
- [20] S. Karimoto and M. Naito, *Appl. Phys. Lett.* **84**, 2136 (2004).
- [21] S. Hu, Z. Yue, J. S. Lim, S. J. Callori, J. Bertinshaw, A. Ikeda-Ohno, T. Ohkochi, C. H. Yang, X. Wang, C. Ulrich, and J. Seidel, *Adv. Mater. Interfaces* **2**, 1500012 (2015).
- [22] J. H. Haeni, P. Irvin, W. Chang, R. Uecker, P. Reiche, Y. L. Li, S. Choudhury, W. Tian, M. E. Hawley, B. Craig, A. K. Tagantsev, X. Q. Pan, S. K. Streiffer, L. Q. Chen, S. W. Kirchoefer, J. Levy, and D. G. Schlom, *Nature (London)* **430**, 758 (2004).
- [23] J. Schubert, O. Trithaveesak, A. Petraru, C. L. Jia, R. Uecker, P. Reiche, and D. G. Schlom, *Appl. Phys. Lett.* **82**, 3460 (2003).
- [24] H. Meley, Karandeep, L. Oberson, J. de Bruijckere, D. T. L. Alexander, J. M. Triscone, P. Ghosez, and S. Gariglio, *Apl Mater.* **6**, 069901 (2018).
- [25] R. J. Paull, Z. R. Mansley, T. Ly, L. D. Marks, and K. R. Poeppelmeier, *Inorg. Chem.* **57**, 4104 (2018).
- [26] R. J. Paull, T. Ly, Z. R. Mansley, K. R. Poeppelmeier, and L. D. Marks, *Crystals* **9**, 218 (2019).
- [27] R. Uecker, R. Bertram, M. Brutzam, Z. Galazka, T. M. Gesing, C. Guguschev, D. Klimm, M. Klupsch, A. Kwasniewski, and D. G. Schlom, *J. Cryst. Growth* **457**, 137 (2017).
- [28] R. Uecker, B. Velickov, D. Klimm, R. Bertram, M. Bernhagen, M. Rabe, M. Albrecht, R. Fornari, and D. G. Schlom, *J. Cryst. Growth* **310**, 2649 (2008).
- [29] J. E. Kleibeuker, G. Koster, W. Siemons, D. Dubbink, B. Kuiper, J. L. Blok, C. H. Yang, J. Ravichandran, R. Ramesh, J. E. ten Elshof, D. H. A. Blank, and G. Rijnders, *Adv. Funct. Mater.* **20**, 3490 (2010).
- [30] J. E. Kleibeuker, B. Kuiper, S. Harkema, D. H. A. Blank, G. Koster, G. Rijnders, P. Tinnemans, E. Vlieg, P. B. Rossen, W. Siemons, G. Portale, J. Ravichandran, J. M. Szepieniec, and R. Ramesh, *Phys. Rev. B* **85**, 165413 (2012).
- [31] R. Dirsyte, J. Schwarzkopf, G. Wagner, R. Fornari, J. Lienemann, M. Busch, and H. Winter, *Surf. Sci.* **604**, L55 (2010).
- [32] A. Biswas, C. H. Yang, R. Ramesh, and M. H. Jeong, *Prog. Surf. Sci.* **92**, 117 (2017).
- [33] Z. R. Mansley, C. A. Mizzi, P. Koirala, J. Wen, and L. D. Marks, *Phys. Rev. Mater.* **4**, 045003 (2020).
- [34] T. Ly, J. G. Wen, and L. D. Marks, *Nano Lett.* **18**, 5186 (2018).
- [35] P. Blaha, K. Schwarz, G. K. H. Madsen, D. Kvashnicka, J. Luitz, R. Laskowsji, F. Tran, and L. D. Marks, *An Augmented Plane Wave + Local Orbitals Program for Calculating Crystal Properties Technology* (Universitat Wien, Austria, 2018).
- [36] P. Blaha, K. Schwarz, F. Tran, R. Laskowski, G. K. H. Madsen, and L. D. Marks, *J. Chem. Phys.* **152**, 074101 (2020).
- [37] P. Novak, J. Kunes, L. Chaput, and W. E. Pickett, *Phys. Status Solidi B* **243**, 563 (2006).
- [38] F. Tran, J. Kunes, P. Novak, P. Blaha, L. D. Marks, and K. Schwarz, *Comput. Phys. Commun.* **179**, 784 (2008).
- [39] J. P. Perdew, A. Ruzsinszky, G. I. Csonka, O. A. Vydrov, G. E. Scuseria, L. A. Constantin, X. Zhou, and K. Burke, *Phys. Rev. Lett.* **100**, 136406 (2008).
- [40] C. A. Mizzi, P. Koirala, and L. D. Marks, *Phys. Rev. Mater.* **2**, 025001 (2018).
- [41] P. Koirala, C. A. Mizzi, and L. D. Marks, *Nano Lett.* **18**, 3850 (2018).
- [42] C. A. Mizzi, P. Koirala, A. Gulec, and L. D. Marks, *Ultramicroscopy* **203**, 119 (2019).
- [43] See Supplemental Material at <http://link.aps.org/supplemental/10.1103/PhysRevMaterials.5.125002> for CIFs, additional multislice simulations, a larger scale version of Fig. 2(c), and comparison between ball-and-stick and polyhedral representations of the (110) double layer structure.
- [44] L. D. Marks, *J. Chem. Theory Comput.* **9**, 2786 (2013).
- [45] D. M. Kienzle, A. E. Becerra-Toledo, and L. D. Marks, *Phys. Rev. Lett.* **106**, 176102 (2011).
- [46] S. Cook and L. D. Marks, *J. Phys. Chem. C* **122**, 21991 (2018).
- [47] F. Silly, D. T. Newell, and M. R. Castell, *Surf. Sci.* **600**, 219 (2006).
- [48] J. Ciston, A. Subramanian, D. M. Kienzle, and L. D. Marks, *Surf. Sci.* **604**, 155 (2010).
- [49] M. Oncak, R. Wlodarczyk, and J. Sauer, *J. Phys. Chem. Lett.* **6**, 2310 (2015).
- [50] K. Refson, R. A. Wogelius, D. G. Fraser, M. C. Payne, M. H. Lee, and V. Milman, *Phys. Rev. B* **52**, 10823 (1995).
- [51] A. E. Becerra-Toledo, J. A. Enterkin, D. M. Kienzle, and L. D. Marks, *Surf. Sci.* **606**, 791 (2012).
- [52] A. E. Becerra-Toledo, M. R. Castell, and L. D. Marks, *Surf. Sci.* **606**, 762 (2012).

- [53] Z. R. Mansley, R. J. Paull, L. Savereide, S. Tatro, E. P. Greenstein, A. Gosavi, E. Cheng, J. Wen, K. R. Poeppelmeier, J. M. Notestein, and L. D. Marks, *ACS Catalysis* **11**, 11921 (2021).
- [54] L. D. Marks, A. N. Chiaramonti, S. U. Rahman, and M. R. Castell, *Phys. Rev. Lett.* **114**, 226101 (2015).
- [55] L. A. Crosby, R. M. Kennedy, B. R. Chen, J. Wen, K. R. Poeppelmeier, M. J. Bedzyk, and L. D. Marks, *Nanoscale* **8**, 16606 (2016).
- [56] L. A. Crosby, B. R. Chen, R. M. Kennedy, J. G. Wen, K. R. Poeppelmeier, M. J. Bedzyk, and L. D. Marks, *Chem. Mater.* **30**, 841 (2018).